Ice I$_h$−Water Interfacial Free Energy of Simple Water Models with Full Electrostatic Interactions

Ruslan L. Davidchack,*,[†] Richard Handel,[†] Jamshed Anwar,[‡] and Andrey V. Brukhno[§]

[†]Department of Mathematics, University of Leicester, Leicester LE1 7RH, United Kingdom
[‡]Computational Biophysics, Institute of Life Sciences Research, University of Bradford, West Yorkshire BD7 1DP, United Kingdom
[§]Centre for Molecular Nanoscience (CMNS), University of Leeds, Leeds LS2 9JT, United Kingdom

ABSTRACT: We employ the cleaving approach to calculate directly the ice I$_h$−water interfacial free energy for the simple models of water, TIP4P, TIP4P-Ew, and TIP5P-E, with full electrostatic interactions evaluated via the Ewald sums. The results are in good agreement with experimental values, but lower than previously obtained for TIP4P-Ew and TIP5P-E by indirect methods. We calculate the interfacial free energies for basal, prism, and {11$\bar{2}$0} interfaces and find that the anisotropy of the TIP5P-E model is different from that of the TIP4P models. The effect of including full electrostatic interactions is determined to be smaller than 10% compared to the water models with damped Coulomb interactions, which indicates that the value of the ice−water interfacial free energy is determined predominantly by the short-range packing interaction between water molecules. We also observe a strong linear correlation between the interfacial free energy and the melting temperature of different water models.

1. INTRODUCTION

The solid−liquid interfacial free energy, γ_{sl}, is the key thermodynamic quantity controlling the processes of homogeneous crystal nucleation and growth from melt.[1] Its anisotropy, i.e., the dependence on the orientation of the interface with respect to the crystal lattice, is largely responsible for the morphology of dendritic growth.[2] Therefore, the ability to accurately determine γ_{sl} and its anisotropy, either by experimental measurement or by theoretical calculation, is of considerable fundamental and technological interest. The experimental study of solid−liquid interfacial systems is very challenging, and despite a rapid growth of activity in this area in recent years, the accuracy of the obtained results is not yet satisfactory. At the same time, several methods have been proposed in recent years to calculate γ_{sl} in computer simulations of model systems. They include the capillary fluctuation method,[3−5] the cleaving method,[6−10] and a more recent method based on metadynamics simulations.[11] These methods are sufficiently accurate to resolve the anisotropy of γ_{sl} and have been applied to a variety of model systems, including hard and soft spheres, the hard-dumbbell system,[12] the Lennard-Jones system,[8,11] embedded atom models of many metal and alloy systems, the Stillinger−Weber model of silicon,[13] and succinonitrile (SCN).[14]

In our recent work,[10] the cleaving method was adapted for the calculation of γ_{sl} in a system consisting of molecules, i.e., where the crystal structure is determined not just by the position, but also by the orientation of the molecules. As a test of the method, we calculated the interfacial free energy of {0001} (basal), {1$\bar{1}$00} (prism), and {11$\bar{2}$0} interfaces of the TIP4P model of water with truncated electrostatic interactions.

In the study presented here, we have chosen to use this method to calculate γ_{sl} for several other models of water. Our choice was guided by the fact that water is one of the most widely simulated substances, especially in biomolecular applications, and it is important to characterize as fully as possible various models of water used in such simulations. In most current applications of molecular simulations involving water, the long-range electrostatic interactions between the charge sites are fully included (i.e., without truncation) using, for example, Ewald sums. A majority of the recently proposed water models are parametrized for use with full electrostatic interactions, and even some of the older models, such as TIP4P and TIP5P, which were originally parametrized to be used with the truncated electrostatic interactions, have now been reparametrized for use with full electrostatics.[15,16] Therefore, it makes sense to include in our investigation water models with full electrostatic interactions. We have chosen to calculate γ_{sl} for three such models. The first model is the original TIP4P model[17] with the full electrostatic interactions. The melting temperature of this model was determined to be 230 K. This should be compared to the 219 K melting temperature of the truncated TIP4P model we used in our previous calculation.[10] By comparing results for this model and the previous one, we can determine the influence of employing full electrostatic interactions on the interfacial free energy. The other two models are TIP4P-Ew[15] and TIP5P-E,[16] adapted from the original TIP4P and TIP5P models as mentioned above. The reason we chose these two models is that there was a recent work estimating γ_{sl} for these models indirectly from the superheating−undercooling simulations,[18] so our results will also allow us to make a comparison between the two approaches.

2. CLEAVING METHOD

In the cleaving method[6−10] the solid−liquid interfacial free energy is determined directly from the reversible work required

---

to splice a solid and a liquid system equilibrated at the coexistence conditions into a single system where the two phases are separated by a planar interface. The splicing transformation is performed in four basic steps:

Step 1. "Cleave" the solid system by gradually introducing an external "cleaving potential" at a specific position (the "cleaving plane") between two adjacent crystal layers of a specified orientation.

Step 2. Cleave the liquid system with the same potential to induce the formation of layers compatible with those in the crystal.

Step 3. Rearrange the boundary conditions to merge the solid and liquid systems, while maintaining the cleaving potential.

Step 4.. Remove the cleaving potential from the combined interfacial system.

The cleaving potential for systems consisting of rigid molecules has been developed in our previous work.[10] For a molecule with center-of-mass coordinates $\mathbf{r}$ and orientational coordinates $\mathbf{q}$, the cleaving potential is designed in the form

$$\Phi(\mathbf{r}, \mathbf{q}) = \sum_j \phi(|\mathbf{r}-\mathbf{R}_j|)\theta(\mathbf{q}, \mathbf{Q}_j) \tag{1}$$

where $\mathbf{R}_j$ are the positions of the molecules in layers of the ideal crystal structure at the cleaving plane and $\mathbf{Q}_j$ are the desired orientations of these molecules. The radial part of the cleaving potential is an attracting "potential well" function, $\phi(r)$, with a minimum (negative) value $-d_w$ (the "well depth") at $r = 0$ and a finite range r_w, i.e., $\phi(r \geq r_w) = 0$. In this work we employ a simple polynomial function

$$\phi(r) = d_w[(r/r_w)^2 - 1]^3 \tag{2}$$

for $r < r_w$. The orientational part takes the form

$$\theta(\mathbf{q}, \mathbf{Q}) = \mathbf{n}(\mathbf{q})\cdot\mathbf{n}(\mathbf{Q}) \tag{3}$$

where $\mathbf{n}$ is a unit vector directed from the oxygen to the midpoint of the hydrogens, i.e., along the dipole moment of the molecule.

During step n of the cleaving method, the reversible work, W_n, is calculated, and the solid–liquid interfacial free energy is given by

$$\gamma_{sl} = A^{-1} \sum_{n=1}^{4} W_n \tag{4}$$

where A is the area of the created interface. The reversible work W_n is calculated using a standard coupling parameter approach[19] wherein the total potential energy of the system depends on the coupling parameter λ in such a way that changing the parameter value from $\lambda = 0$ to $\lambda = 1$ transforms the system from its initial to its final state. In the thermodynamic integration formulation of the coupling parameter approach, W_n is given by

$$W_n = \int_0^1 \langle \partial U_n / \partial \lambda \rangle_\lambda \, d\lambda \tag{5}$$

where $\langle ... \rangle_\lambda$ denotes an average over the equilibrium state at a fixed value of λ. The λ-dependent potential energy of the system in each step is defined as follows:

step 1: $U_1(\lambda) = U_s + \lambda\Phi_s$

step 2: $U_2(\lambda) = U_1 + \lambda\Phi_1$

step 3: $U_3(\lambda) = (1 - \lambda)(U_s + U_1) + \lambda U_{sl} + \Phi_s + \Phi_1$

step 4: $U_4(\lambda) = U_{sl} + (1 - \lambda)(\Phi_s + \Phi_1)$

where U_s, U_l, and U_{sl} are the potential energies of the solid, liquid, and combined systems, respectively, and Φ_s and Φ_l are the cleaving potentials in the solid and liquid systems.

3. NONEQUILIBRIUM WORK MEASUREMENTS

To calculate the reversible work in each step of the cleaving process, we have chosen to use the nonequilibrium work measurement approach, which we have successfully used in the past.[10,20] This approach was pioneered by Jarzynski[21] and further developed to provide a reliable and accurate estimation of the reversible work.[22,23] Within this approach the coupling parameter λ in eq 5 is changed from 0 to 1 in a finite switching time t_s, so $\lambda(t)$ is a continuous function such that $\lambda(0) = 0$ and $\lambda(t_s) = 1$. The nonequilibrium work, $\mathcal{W}$, is measured according to the formula

$$\mathcal{W} = \int_0^{t_s} \frac{\partial U(\Gamma(t); \lambda)}{\partial \lambda} \dot{\lambda}(t) \, dt \tag{6}$$

where $\Gamma(t)$ is a phase space trajectory (generated by molecular dynamics or Monte Carlo). The speed of change of the coupling parameter, $\dot{\lambda}(t)$, defines the protocol of the switching process and can be tailored to slow the process over regions with weak ergodicity. This ability to vary the switching speed is a useful device for concentrating computing time on the problematic regions of the transformation path. If the trajectory starts from an equilibrated state at temperature T, then, for a given switching protocol, the canonical distribution of the initial states (proportional to $\exp(-\beta U(\lambda = 0))$, where $\beta = 1/k_BT$) induces a probability distribution of nonequilibrium work measurements $P(\mathcal{W})$. If we run several such trajectories, each starting from an independent equilibrium configuration, then we can estimate averages over this distribution. In particular, the average of the exponent of the nonequilibrium work measurements is related to the reversible work W as follows:[21,24]

$$\langle e^{-\beta\mathcal{W}} \rangle = e^{-\beta W} \tag{7}$$

where brackets denote the average over $P(\mathcal{W})$.

The estimator for W based on eq 7 is not very efficient, since it depends heavily on the tail of the distribution $P(\mathcal{W})$, which is not sampled sufficiently well unless a very large number of trajectories are simulated. A more efficient estimator can be derived if it is also possible to run the switching process in reverse. Such a process starts from an initial state sampled from the canonical distribution proportional to $\exp(-\beta U(\lambda = 1))$ and follows the switching protocol of the forward process in reverse (as if running backward in time). It turns out[25] that the forward (f) and reverse (r) nonequilibrium work distributions are related by the formula

$$P_f(\mathcal{W}) = e^{\beta(\mathcal{W}-W)} P_r(-\mathcal{W}) \tag{8}$$

and thus, the reversible work can be estimated from the formula

$$e^{-\beta W} = \frac{\langle h(\mathcal{W}) \rangle_f}{\langle h(-\mathcal{W}) e^{-\beta\mathcal{W}} \rangle_r} \tag{9}$$

where the brackets with subscripts f and r denote averages over distributions $P_f(\mathcal{W})$ and $P_r(\mathcal{W})$, respectively, and $h(\mathcal{W})$ is any bounded function. If we run n_f forward and n_r reverse trajectories, then it can be shown that the best estimator for W (i.e., an asymptotically unbiased estimator with minimum variance[26,27]) is obtained when $h(\mathcal{W})$ has the form

$$h(\mathcal{W}) = \left(1 + \frac{n_f}{n_r}e^{\beta(\mathcal{W}-W)}\right)^{-1}$$

$$(10)$$

In practice, this means that W is given by the (unique) solution of the nonlinear equation

$$\sum_{i=1}^{n_f} \frac{1}{1 + e^{\beta(M+\mathcal{W}_i-W)}} = \sum_{j=1}^{n_r} \frac{1}{1 + e^{-\beta(M+\mathcal{W}_j-W)}}$$

$$(11)$$

where $M = k_B T \ln(n_f/n_r)$ and, for convenience of the notation, the values of the reverse work are taken with a minus sign. This equation is identical to the acceptance ratio equation[19] derived by Bennett[28] for the case of instantaneous switching between two equilibrium states. Therefore, we will refer to the nonequilibrium work measurement method that utilizes eq 11 as the Bennett acceptance ratio (BAR) method.[26,27] The variance of the reversible work obtained from eq 11 can be estimated according to the formula

$$\sigma_W^2 = \frac{1}{\beta^2}\left[\left(\sum_i \frac{1}{2 + 2\cosh[\beta(M + \mathcal{W}_i - W)]}\right)^{-1} - \left(\frac{1}{n_f} + \frac{1}{n_r}\right)\right]$$

$$(12)$$

where the sum is over all work measurements, both forward and reverse.

4. IMPROVING REVERSIBILITY OF THE TRANSFORMATION PATH

For the BAR method to yield accurate estimates of the reversible work, the distributions $P_f(\mathcal{W})$ and $P_r(-\mathcal{W})$ need to have some overlap. This means that the forward and reverse trajectories should not be driven too far from the regions of phase space typically sampled by the equilibrium trajectories. One way to achieve this is to increase the switching time t_s and use a relatively strong coupling between the system and the thermostat. However, if during the switching process the system encounters a high free energy barrier, then the required switching time is prohibitively long and sufficient overlap of the two distributions cannot be achieved within a reasonable computational time.

As has been found in previous studies,[8–10,20] such a situation occurs in step 2 of the cleaving method. In the process of creating a structural ordering in the liquid under the influence of an external potential at the coexistence conditions, the system needs to cross a high free energy barrier associated with the nucleation of the ordered structure. As a result, the forward and reverse trajectories take very different paths in the phase space, resulting in the appearance of a hysteresis loop. This is illustrated in Figure 1, where we show the values of $\partial U/\partial \lambda$, which appears in eq 6, plotted against λ for five forward and five reverse trajectories with $t_s = 1$ ns. The integral of each function gives approximately the nonequilibrium work performed along each trajectory, as defined in eq 6. It is clear that the values for
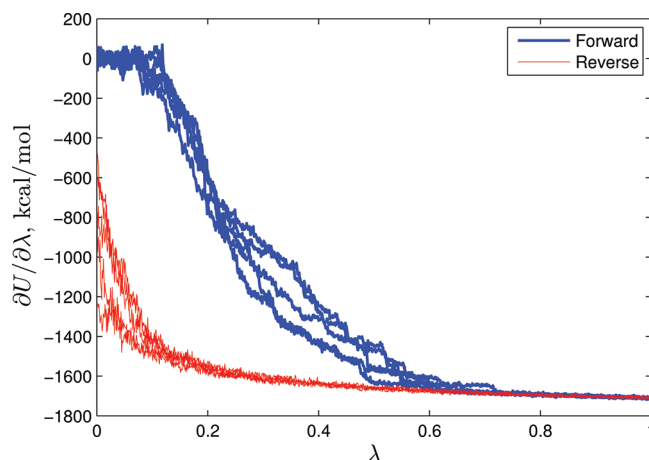

Figure 1. Integrand in the nonequilibrium work measurement, eq 6, plotted against λ for five forward and five reverse trajectories in step 2 of the cleaving process. The large hysteresis between the forward and reverse trajectories makes it difficult to accurately estimate the reversible work during this step.

forward and reverse work measurements differ significantly, so there is virtually no overlap between the two distributions. Increasing the switching time to 2 ns has essentially no effect on the distance between the two distributions, so a different approach to dealing with the hysteresis problem is required in this case.

The reason behind the persistence of the hysteresis in step 2 is as follows. Being at the solid–liquid coexistence conditions and given a suitable seed structure (provided in this case by the cleaving potential), the liquid readily forms ordered metastable structures that persist for a long time even when the seed structure is removed (which happens during the reverse transformation in step 2). Such structures are much less stable and decay much faster when the liquid is not at the coexistence conditions. Therefore, as we have shown in our previous studies,[8–10,20] the hysteresis problem in step 2 can be significantly reduced by cleaving the liquid system in conditions away from the coexistence. For the ice–water system, a simple solution is to perform step 2 at a temperature higher than the melting temperature T_m. Note that, in the canonical ensemble, increasing the temperature of the system is thermodynamically equivalent to scaling down the interaction potential.[29] Scaling the potential is more convenient within the cleaving method, since it can be achieved via the coupling parameter approach simply by multiplying the intermolecular interaction potential by a coupling parameter λ, i.e., $U(\lambda) = \lambda U_l$, where U_l is the full interaction potential of the liquid system. The work performed during the potential scaling is given by

$$W = \int_1^{\lambda_s} \langle U_l \rangle_\lambda \, d\lambda$$

$$(13)$$

and, just like for all other steps in the cleaving process, can be calculated using the nonequilibrium work measurements.

As can be seen in Figure 2, when the cleaving wells are introduced into the liquid water system with the potential scaled by a factor $\lambda_s = 0.7$, there is essentially no hysteresis. The forward and reverse nonequilibrium distributions have sufficient overlap for the BAR method to produce reliable results. While the total switching time is equal to 1 ns as in Figure 1, we also vary $\dot{\lambda}(t)$, which appears in eq 6, to improve sampling in the region of potential hysteresis. In particular, we
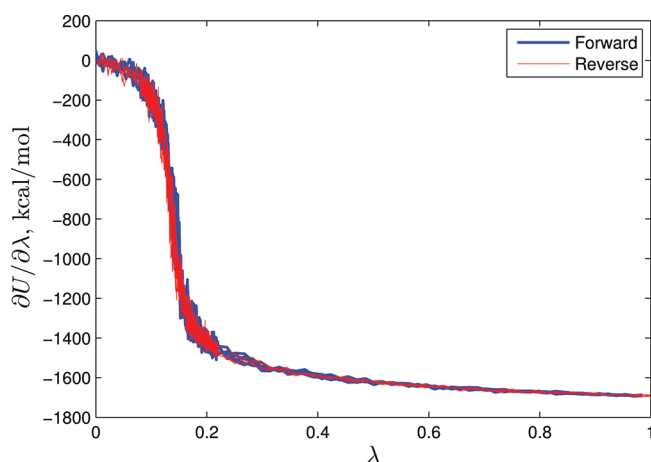
Figure 2. Same as Figure 1 but with step 2 performed on the liquid water system with the intermolecular interaction potential scaled down by a factor of 0.7. Five forward and five reverse trajectories are plotted. The large overlap between the forward and reverse trajectories allows accurate estimation of the reversible work.

use piecewise constant $\dot{\lambda}(t)$ with 0.85 ns taken to change λ from 0 to 0.22 and the remaining 0.15 ns to change λ from 0.22 to 1. We have varied $\dot{\lambda}(t)$ in this way in several other places throughout the cleaving method, wherever we found regions with large differences between the forward and reverse measurements.

The reversible work of scaling and restoring the intermolecular potential must be measured and taken into account when estimating the reversible work in step 2. To use the BAR method for this calculation, we also require that the forward and reverse distributions overlap. As can be seen in Figure 3, this requirement is easily satisfied when the potential
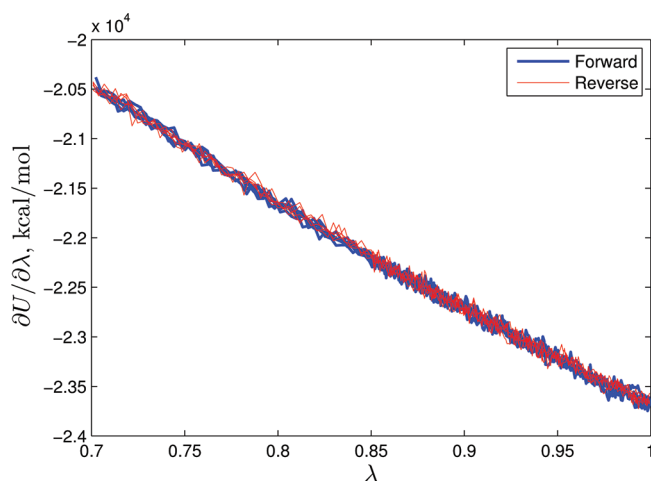

Figure 3. Integrand in the nonequilibrium work measurement, eq 13, with $\lambda_s = 0.7$, plotted against λ for five forward and five reverse trajectories in the process of scaling the water−water interaction potential from full strength to 70%.

is scaled down from 100% to 70%, but when the potential is scaled back to 100% after the introduction of the cleaving wells, the reversibility of the transformation is not as good. As can be seen in Figure 4, the forward and reverse trajectories visibly differ for λ between 0.85 and 1. While this hysteresis is not as severe as in Figure 1, it still leads to the deterioration of the BAR estimator. Increasing the switching time somewhat
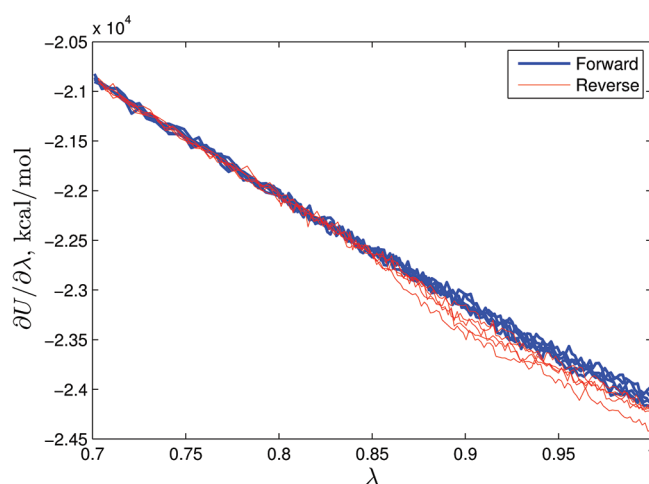

Figure 4. Same as Figure 3 but for the process of scaling the water−water interaction potential back to full strength after the introduction of the cleaving wells. Five forward and five reverse trajectories are plotted. The small hysteresis observed for λ between 0.85 and 1 is caused by the formation of additional ice layers adjacent to the layers formed over the cleaving wells.

improves the results, but not sufficiently to warrant the additional computational effort.

We investigated the origin of the persistent difference between forward and reverse trajectories in Figure 4 and found that it is caused by the formation of additional ice layers adjacent to the layers formed over the cleaving wells. These layers take a relatively long time to form and melt away when the water potential is scaled to about 85%. The formation of additional ice layers also has a detrimental effect on the reversibility of step 3. To improve reversibility in steps 2 and 3, we have modified the transformation path as follows: after the cleaving wells are introduced into the liquid water with a 70% intermolecular potential, the potential is restored only to 85%. Step 3 is then performed with the water−water interaction potential at 85% and ice−ice and ice−water interactions at full strength. Since the ice layers formed at the cleaving wells in step 2 prevent molecules from crossing the cleaving plane, there is no ambiguity about the labeling of molecules as either ice or liquid water. The water potential is restored to full strength during step 4 (described below). With such a modification, the formation of additional layers is prevented, since liquid water is effectively maintained at a temperature about 20% above melting.

Finally, we need to tackle the hysteresis problem in step 4.[10,20] It stems from the difficulty of starting the reverse trajectories from equilibrated states with positions of the cleaving planes precisely aligned with the positions of the ice−water interfaces. At the end of step 4, when the cleaving wells are completely removed from the system, the two interfaces are free to move away from their original positions without disturbing the system equilibrium. This happens when thermal fluctuations cause freezing of the water at one of the interfaces and, at the same time, melting of ice at the other interface. If the cleaving planes are not placed precisely at the locations of the interfaces at the start of the reverse switching process, then one set of the cleaving wells is inserted predominantly within the ice and the other within the liquid water. The final state of the reverse switching process is obviously not the same as the

state at the start of the forward switching process, and therefore, the conditions of the BAR method are not satisfied.

To overcome this problem, we perform step 4 in two stages. First, we use the BAR method to determine work required to reduce the well strength to 25% and simultaneously restore the water potential to full strength. The 25% value was determined to be the lowest possible at which the ice—water interfaces still remain locked in the positions determined by the positions of the wells, so there is no problem with initializing the reverse trajectories. Second, the removal of the remaining 25% of the wells is performed in the forward direction only. To account for the bias inherent in the one-way nonequilibrium switching, the forward trajectories are run at three different speeds (switching times of 0.8, 1.2, and 2.4 ns) and the average nonequilibrium works are extrapolated to the infinite switching time. In addition, exponential averages are calculated on the basis of eq 7 at each speed. We found that the exponential averages and the extrapolated value were consistent within the estimated statistical errors.

Combining the above-discussed modifications of the four-step cleaving process, we arrive at the following cleaving transformation path:

Step 1: Introduce cleaving wells into the ice system.
Step 2a: Scale the intermolecular interaction potential in the liquid water system from 100% to 70%.
Step 2b: Introduce cleaving wells into the liquid water system at a 70% interaction potential (effectively at $1.42T_m$).
Step 2c: Scale the intermolecular interaction potential in the liquid water system from 70% to 85% while keeping constant the strength of the cleaving wells.
Step 3: Rearrange the boundary conditions to combine ice and water systems with the water—water interactions at 85% and ice—ice and ice—water interactions at full strength.
Step 4a: Reduce the well strength to 25% while simultaneously restoring the water—water potential to full strength.
Step 4b: Remove the remaining 25% of the well strength (forward direction only).

5. ELECTROSTATIC INTERACTIONS

Ewald summation is one of the most commonly used approaches to evaluating the long-range electrostatic interactions. Within this approach, the electrostatic potential energy is written as a sum of two terms:

$$U_{Coul} = U_{short-range} + U_{Fourier} \qquad (14)$$

where

$$U_{short-range} = \frac{1}{4\pi\varepsilon_0} \sum_{n<j} \frac{q_j q_n}{r_{nj}} \mathrm{erfc}(\alpha r_{nj}) \qquad (15)$$

is the Coulomb potential function scaled by a rapidly decaying complementary error function, which results from the screening of the point charges by compensating Gaussian charge distributions surrounding each charge, and

$$U_{Fourier} = \frac{1}{2V_0\varepsilon_0} \sum_{\mathbf{k}\neq 0} k^{-2} e^{-k^2/(2\alpha)^2} |\sum_j q_j e^{-i\mathbf{k}\cdot\mathbf{r}_j}|^2 \qquad (16)$$

which describes the potential energy of the Gaussian charge distributions expressed as a rapidly decaying sum over reciprocal lattice vectors $\mathbf{k}$ in Fourier space. In our simulations we set $\alpha = 0.26$ Å^{-1} and smoothly truncate the short-range

potential at 8.5 Å as described in ref 15. We also limit the Fourier space sum over the reciprocal lattice vectors with $k < k_{max} = 1.15$ Å^{-1}.

The computational cost of Ewald sums can be significant, particularly for large systems. In the case of the combined ice—water system, consisting of about 4000 molecules, we observed an increase in computation time by a factor of about 10 compared with smooth truncation at 10 Å.

At the same time, since each water molecule has zero total charge, the electrostatic interactions are well screened in this system and the contribution to the interaction potential and forces of the Fourier space components of the Ewald sums is very small compared with that of the real-space terms. For example, for a system at the ice—water coexistence conditions, the magnitude of the Fourier term in the potential energy is less than 0.1% of the total potential energy magnitude, while the contribution from this term to the pressure is less than 1%. Therefore, the Fourier space part of the Ewald sums potential adds only a small perturbation to the system interacting via $U_{short-range}$. This is not surprising since the water model with the interaction potential given solely by $U_{short-range}$ is similar to the *damped Coulomb* potential of Wolf et al.,[30,31] which provides a much better approximation to the full electrostatic interaction compared to the truncated potential.

These considerations allow us to adopt a more efficient approach to calculating the interfacial free energy for systems with Ewald sums: We first transform the full electrostatic ice and liquid water systems into the systems interacting only with $U_{short-range}$ (referred to hereafter as "short-range water" model) by gradually switching off the Fourier part of the Ewald sums, then perform the cleaving process on the short-range water system, and finally gradually restore the Fourier part in the combined ice—water system. The additional work of switching the Fourier term on and off is readily calculated using the same coupling parameter approach as in the cleaving method. The λ-dependent potential energy is simply given by

$$U(\lambda) = U_{short-range} + \lambda U_{Fourier} \qquad (17)$$

Thus, the approach we adopted for calculating γ_{sl} in the system with Ewald sums consists of the following steps:

- Switch off the Fourier term (by changing λ from 1 to 0 in eq 17) in separate ice and liquid water systems equilibrated at the melting temperature. Calculate the reversible work W_{off}.
- Use the cleaving method presented in section 4 to calculate the ice—water interfacial free energy of the short-range water model.
- Switch the Fourier term back on in the combined ice—water system. Calculate the reversible work W_{on}.

The interfacial free energy of the system with full electrostatic interaction is then given by

$$\gamma_{sl} = \gamma_{sl}|_{\lambda=0} + A^{-1}(W_{on} - W_{off}) \qquad (18)$$

Note that in the above approach we assume that the melting temperature of the short-range water model is the same as that of the model with full electrostatic interactions. Indeed, we have performed direct coexistence simulations[32,33] of the short-range water models corresponding to each of the three water models we have investigated and found that the melting temperatures were the same within the statistical uncertainty of about 2 K. However, this is not a limitation of our approach, which can easily be extended to the case when the melting temperatures

of the two models are not equal. For example, if the melting temperature of the short-range water model were determined to be T_m', which was different from the melting temperature, T_m, of the full model, then we could modify the λ-dependent potential energy in eq 17 as follows:

$$U(\lambda) = [\lambda + (1 - \lambda)T_m/T_m']U_{\text{short-range}} + \lambda U_{\text{Fourier}} \quad (19)$$

This modification ensures that the melting temperature of the model with $\lambda = 0$ is equal to T_m.

The transformations from the full electrostatics to short-range water model and back can be accomplished using the same nonequilibrium methods as described above for the cleaving method steps. Since these transformations are relatively straightforward (i.e., the forward and reverse work distributions have significant overlap for relatively short switching times), the additional computation time is negligible compared to the time saved in the rest of the process. Overall, we obtain a speed-up by a factor of about 7, taking into account the extra steps in transforming between the two models.

6. COMPUTATIONAL DETAILS

Calculations were performed on three models: TIP4P,[17] TIP4P-Ew,[15] and TIP5P-E.[16] For each model, the ice I_h–water interfacial free energies were calculated for the {0001} (basal), {1$\bar{1}$00} (prism), and {11$\bar{2}$0} interfaces. We employed molecular dynamics simulation, with the velocity Verlet algorithm for translational degrees of freedom and the quaternion-based algorithm NO_SQUISH[34] for rotational ones. All simulations were done in the NVT ensemble. The temperature was controlled by a Langevin thermostat applied to both translational and rotational degrees of freedom. We found that the Langevin thermostat, with its independent thermalization of each degree of freedom, was superior to the Nosé–Hoover thermostat, which we used in the previous study,[10] especially in step 3, where two noninteracting systems are combined into one. We used the Langevin A algorithm[35] with friction parameters $\gamma = 5$ ps^{-1} and $\Gamma = 15$ ps^{-1}, which provided a maximum speed of system equilibration. We used a relatively large time step of 4 fs, which was determined to be optimal in terms of sampling speed and accuracy.[36]

For each cleaving step, 10 trajectories in each direction were run. The ice I_h crystal for each trajectory was given its own distinct proton-disordered structure using an algorithm devised by Buch et al.[37] The ice systems contained 2160 molecules for the basal and prism orientations and 2400 for the {11$\bar{2}$0} orientation. The simulation cell dimensions were $L_x \approx 40$ Å, $L_y \approx 40$ Å, and $L_z \approx 45$ Å. The liquid water systems had the same number of molecules and exactly the same L_x and L_y dimensions, while L_z was scaled by the ratio of ice to liquid water densities.

The ice I_h melting temperatures for each model were determined in the direct ice–water coexistence simulations[32,33] of up to 10 ns. The ice and liquid water densities were calibrated in separate simulations where the size of the simulation box (independently for each direction in the case of the ice system) was adjusted to yield approximately zero components of the pressure tensor. The melting temperatures, densities, enthalpies, and latent heats of fusion for the three models are summarized in Table 1. The values for model systems agree within statistical errors with those published previously.[38] The experimental values are taken from ref 38.

Table 1. Ice I_h–Water Coexistence Properties at Zero Pressure for Water Models with Full Electrostatic Interactions[a]

	TIP4P	TIP4P-Ew	TIP5P-E	exptl
T_m, K	230	245	270	273
ρ_s, kg/m^3	938	935	966.5	917
ρ_l, kg/m^3	1000	992	987	999
H_s, kcal/mol	−12.02	−13.05	−12.17	
H_l, kcal/mol	−10.98	−11.97	−10.45	
ΔH, kcal/mol	1.04	1.08	1.72	1.44

[a]Listed are the melting temperature, T_m, densities of ice I_h, ρ_s, and liquid water, ρ_l, enthalpies of ice I_h, H_s, and liquid water, H_l, and latent heat of fusion, ΔH. The values for the real water are shown for comparison.

As was mentioned earlier, the cleaving plane in step 1 is placed between two adjacent layers of the ideal ice crystal. Due to the introduction of the external well potential, the linear momentum of the system is no longer conserved, so the crystal layers can drift with respect to the cleaving plane, disrupting the cleaving transformation process and introducing systematic errors in the work measurements. To prevent such a drift, a layer of ice molecules on the opposite side of the system from the cleaving plane is pinned relative to the simulation box. Each molecule in the pinned layer is attached by its center of mass to its ideal crystal position by a harmonic spring. The strength of the spring is set to 4 kcal/(mol Å^2), a value determined to be as small as possible while remaining effective in preventing the drift. This pinning potential remains in place throughout the cleaving process and, given that the crystal system is sufficiently large in the direction normal to the interface, has no effect on the computed interfacial free energies.

The parameters of the cleaving well potential, eq 2, are $d_w = 10$ kcal/mol and $r_w = 2$ Å. The switching times t_s for different steps of the cleaving transformation range from 0.2 to 2.4 ns, depending on the difficulty of obtaining sufficient overlap between the forward and reverse work distributions.

7. RESULTS AND DISCUSSION

The results of our calculations for the three models with full electrostatic interactions and three different interface orientations are shown in Table 2. The values of γ_{sl} averaged over the

Table 2. Ice I_h–Water Interfacial Free Energies (mJ/m^2) for Different Crystal Orientations of Water Models with Full Electrostatic Interactions[a]

	TIP4P	TIP4P-Ew	TIP5P-E
basal	24.5(6)	25.5(7)	27.8(9)
prism	27.6(7)	28.9(8)	27.4(8)
{11$\bar{2}$0}	27.5(7)	28.3(7)	31.6(7)

[a]The numbers in parentheses indicate the uncertainty in the last digit shown with a 95% confidence level.

three orientations, 26.5(4), 27.6(5), and 28.9(5) mJ/m^2 for TIP4P, TIP4P-Ew, and TIP5P-E, respectively, are in surprisingly good agreement with the experimental value[39] of 29.1(8) mJ/m^2, which is widely accepted to be the most accurate experimental result. At the same time, they are much lower than the results[18] obtained for TIP4P-Ew and TIP5P-E models using an indirect approach based on the superheating–undercooling hysteresis method.[40]

Our results are sufficiently precise to resolve the anisotropy of γ_{sl}. They show that the TIP5P-E model has anisotropy properties different from those of the two TIP4P models. In particular, while the free energy of the basal interface is always lower than that of the $\{11\bar{2}0\}$ interface, the value for the prism interface is similar to that of the basal interface for TIP5P-E, but similar to that of the $\{11\bar{2}0\}$ interface for TIP4P and TIP4P-Ew.

It is interesting to compare the Turnbull coefficients for different water models and that for real water. Analyzing the values of γ_{sl} obtained for different materials from nucleation rate measurements, Turnbull found a linear dependence between the interfacial free energy per interface particle and the latent heat of fusion:[41]

$$\gamma_{sl} n_s^{-2/3} = C_T \Delta H \tag{20}$$

where $n_s = \rho_s / m_{H_2O}$ is the number density of the solid phase. The Turnbull coefficient, C_T, was found to be approximately 0.45 for metals (especially close-packed metals) and 0.32 for nonmetallic materials. Using Hardy's value for γ_{sl}, the Turnbull coefficient for water is 0.30. From our results for γ_{sl} averaged over the three orientations and the values of the latent heat of fusion given in Table 1, we obtain the Turnbull coefficients 0.37, 0.36, and 0.24 for TIP4P, TIP4P-Ew, and TIP5P-E, respectively. Thus, the Turnbull coefficient of real water is overestimated by the TIP4P models and underestimated by the TIP5P-E model. This result appears to be primarily related to the fact that, as shown in Table 1, the TIP4P models underestimate the latent heat of fusion while the TIP5P-E model overestimates it.

It is also worth noting that the calculated values of γ_{sl} for various models appear to increase with the increasing melting points of the models. This correlation also extends to our earlier study,[10] where the average interfacial free energy was determined to be 23.9(5) mJ/m^2 for the truncated TIP4P model with the melting temperature $T_m = 219$ K. The linear scaling between the interfacial free energy per interfacial particle and the melting temperature was discussed by Laird,[42] who observed that

$$\gamma_{sl} n_s^{-2/3} = C_L k_B T_m \tag{21}$$

with the coefficient C_L approximately equal to 0.5 for many metals, especially those with the close-packed crystal structure. Note that eq 21 was shown[9] to be exact along the solid–liquid coexistence curves for systems interacting with inverse-power repulsive potentials, $u(r) = \varepsilon(\sigma/r)^n$, for any n, including the case of hard spheres in the limit $n \rightarrow \infty$. Calculating C_L for water, we get 0.79 for real water (using Hardy's value for γ_{sl}) and 0.80, 0.84, 0.82, and 0.77 for truncated TIP4P,[10] TIP4P, TIP4P-Ew, and TIP5P-E, respectively. It is clear that these values are much more consistent than the Turnbull coefficients for the same models, which indicates that eq 21 is better than the Turnbull relation at predicting the ice I_h–water interfacial free energy for various water models. The observation that the linear scaling between γ_{sl} and T_m observed in simple atomic systems also applies to models of water is rather surprising given the complexity of the interaction between water molecules. It certainly would be interesting to investigate the origin of such a scaling and its range of applicability to systems of increasing complexity.

Finally, our approach of switching from models with full electrostatic interactions to the corresponding short-range water models allows us to determine the effect of long-range interactions on the values of γ_{sl}. In Table 3 we show the

Table 3. Difference between γ_{sl} for Models with Full Electrostatic Interactions and γ_{sl} for the Short-Range Water Models[a]

	TIP4P	TIP4P-Ew	TIP5P-E
basal	−0.5(2)	−0.2(2)	−2.4(2)
prism	−0.3(2)	−0.1(2)	−2.3(2)
$\{11\bar{2}0\}$	−0.4(2)	−1.9(2)	−1.5(2)

[a]That is, $\gamma_{sl} - \gamma_{sl}|_{\lambda=0} = A^{-1}(W_{on} - W_{off})$ as defined in eq 18.

difference between the interfacial free energies of the models with full electrostatic interactions and those for the corresponding short-range water models. We see that for all models and interface orientations the inclusion of the full electrostatic interactions leads to a decrease of γ_{sl}. This decrease is relatively small in the TIP4P and TIP4P-Ew models (except for the $\{11\bar{2}0\}$ interface in the TIP4P-Ew model) and larger, but still less than 10%, in the TIP5P-E model. The smallness of this difference indicates that the value of γ_{sl} is largely determined by the short-range packing interaction between water molecules.

8. CONCLUSIONS

We extend the cleaving method to calculate the ice I_h–water interfacial free energy, γ_{sl}, in models of water with full electrostatic interactions evaluated via the Ewald sums. To increase the computational efficiency of the method, we first transform the water models from full to dampened electrostatic interactions (by switching off the reciprocal term in the Ewald sums), then perform the cleaving transformation of the short-range water models, and finally restore the full electrostatic interactions. Besides increased efficiency, such an approach also allows us to estimate the influence of long-range electrostatic interactions on the value of γ_{sl}, which appears to be less than 10% for the TIP5P-E model and even smaller for the TIP4P models, indicating that the value of γ_{sl} is determined primarily by the short-range packing interaction between water molecules. We present results for the interfacial free energies of basal, prism, and $\{11\bar{2}0\}$ interfaces for TIP4P, TIP4P-Ew, and TIP5P-E water models. The results are sufficiently precise to resolve the anisotropy of the interfacial free energy. We find that the basal interface has a lower γ_{sl} than the $\{11\bar{2}0\}$ interface for all models while the prism interface has a value of γ_{sl} similar to that of the basal interface for the TIP5P-E model and similar to that of the $\{11\bar{2}0\}$ interface for the TIP4P models. We also observe a strong linear correlation between the interfacial free energy and the melting temperature of different water models. This correlation is stronger than the one established by Turnbull between the interfacial free energy and the enthalpy of fusion. Finally, note that even though the proposed cleaving method was applied to rigid models of water, it also can be applied without modification to flexible or polarizable models.

■ AUTHOR INFORMATION

Corresponding Author
*E-mail: rld8@leicester.ac.uk.

Notes
The authors declare no competing financial interest.

■ REFERENCES

(1) Woodruff, D. *The Solid-Liquid Interface*; Cambridge University Press: London, 1973.

(2) Hoyt, J. J.; Asta, M.; Karma, A. *Mater. Sci. Eng., R* **2003**, *41*, 121−163.

(3) Hoyt, J. J.; Asta, M.; Karma, A. *Phys. Rev. Lett.* **2001**, *86*, 5530−5533.

(4) Hoyt, J. J.; Asta, M. *Phys. Rev. B* **2002**, *65*, 214106.

(5) Davidchack, R. L.; Morris, J. R.; Laird, B. B. *J. Chem. Phys.* **2006**, *125*, 094710.

(6) Broughton, J. Q.; Gilmer, G. H. *J. Chem. Phys.* **1986**, *84*, 5759−5768.

(7) Davidchack, R. L.; Laird, B. B. *Phys. Rev. Lett.* **2000**, *85*, 4751−4754.

(8) Davidchack, R. L.; Laird, B. B. *J. Chem. Phys.* **2003**, *118*, 7651−7657.

(9) Davidchack, R. L.; Laird, B. B. *Phys. Rev. Lett.* **2005**, *94*, 086102.

(10) Handel, R.; Davidchack, R. L.; Anwar, J.; Brukhno, A. *Phys. Rev. Lett.* **2008**, *100*, 036104.

(11) Angioletti-Uberti, S.; Ceriotti, M.; Lee, P. D.; Finnis, M. W. *Phys. Rev. B* **2010**, *81*, 125416.

(12) Mu, Y.; Song, X. *Phys. Rev. E* **2006**, *74*, 031611.

(13) Apte, P. A.; Zeng, X. C. *Appl. Phys. Lett.* **2008**, *92*, 221903.

(14) Feng, X.; Laird, B. *J. Chem. Phys.* **2006**, *124*, 044707.

(15) Horn, H. W.; Swope, W. C.; Pitera, J. W.; Madura, J. D.; Dick, T. J.; Hura, G. L.; Head-Gordon, T. *J. Chem. Phys.* **2004**, *120*, 9665−9678.

(16) Rick, S. W. *J. Chem. Phys.* **2004**, *120*, 6085−6093.

(17) Jorgensen, W. L.; Chandrasekhar, J.; Madura, J. D.; Impey, R. W.; Klein, M. L. *J. Chem. Phys.* **1983**, *79*, 926−935.

(18) Wang, J.; Tang, Y. W.; Zeng, X. C. *J. Chem. Theory Comput.* **2007**, *3*, 1494−1498.

(19) Frenkel, D.; Smit, B. *Understanding Molecular Simulation*, 2nd ed.; Academic Press: New York, 2002.

(20) Davidchack, R. L. *J. Chem. Phys.* **2010**, *133*, 234701.

(21) Jarzynski, C. *Phys. Rev. Lett.* **1997**, *78*, 2690−2693.

(22) Chipot, C., Pohorille, A., Eds. *Free Energy Calculations: Theory and Applications in Chemistry and Biology*; Springer: Berlin, 2007.

(23) Leliévre, T.; Rousset, M.; Stoltz, G. *Free Energy Computations: A Mathematical Perspective*; Imperial College Press: London, 2010.

(24) Jarzynski, C. *Phys. Rev. E* **1997**, *56*, 5018−5035.

(25) Crooks, G. E. *Phys. Rev. E* **2000**, *61*, 2361−2366.

(26) Shirts, M. R.; Pande, V. S.; Bair, E.; Hooker, G. *Phys. Rev. Lett.* **2003**, *91*, 140601.

(27) Shirts, M. R.; Pande, V. S. *J. Chem. Phys.* **2005**, *122*, 144107.

(28) Bennett, C. H. *J. Comput. Phys.* **1976**, *22*, 245−268.

(29) de Koning, M.; Antonelli, A.; Yip, S. *Phys. Rev. Lett.* **1999**, *83*, 3973−3977.

(30) Wolf, D.; Keblinski, P.; Phillpot, S. R.; Eggebrecht, J. *J. Chem. Phys.* **1999**, *110*, 8254−8282.

(31) Zahn, D.; Schilling, B.; Kast, S. M. *J. Phys. Chem. B* **2002**, *106*, 10725−10732.

(32) Morris, J. R.; Song, X. *J. Chem. Phys.* **2002**, *116*, 9352−9358.

(33) Fernández, R. G.; Abascal, J. L. F.; Vega, C. *J. Chem. Phys.* **2006**, *124*, 144506.

(34) Miller, T. F., III; Eleftheriou, M.; Pattnaik, P.; Ndirango, A.; Newns, D.; Martyna, G. J. *J. Chem. Phys.* **2002**, *116*, 8649−8659.

(35) Davidchack, R. L.; Handel, R.; Tretyakov, M. V. *J. Chem. Phys.* **2009**, *130*, 234101.

(36) Davidchack, R. L. *J. Comput. Phys.* **2010**, *229*, 9323−9346.

(37) Buch, V.; Sandler, P.; Sadlej, J. *J. Phys. Chem. B* **1998**, *102*, 8641−8653.

(38) Vega, C.; Sanz, E.; Abascal, J. L. F. *J. Chem. Phys.* **2005**, *122*, 114507.

(39) Hardy, S. C. *Philos. Mag.* **1977**, *35*, 471−484.

(40) Luo, S.-N.; Strachan, A.; Swift, D. C. *Modell. Simul. Mater. Sci. Eng.* **2005**, *13*, 321−328.

(41) Turnbull, D. *J. Appl. Phys.* **1950**, *21*, 1022−1028.

(42) Laird, B. B. *J. Chem. Phys.* **2001**, *115*, 2887−2888.